ITR/P1-29

Benchmarking ICRF simulations for ITER

R. V. Budny[1], L. Berry[2], R. Bilato[3], P. Bonoli[4], M. Brambilla[3], R. J. Dumont[5], A. Fukuyama[6], R. Harvey[7], E. F. Jaeger[8], E. Lerche[9], C. K. Phillips[1], V. Vdovin[10], J. Wright[4], and members of the ITPA-IOS

[1]*PPPL, P.O. Box 451, Princeton, NJ 08543, USA,* [2]*ORNL, PO Box 2008, Oak Ridge, TN 37831, USA,* [3]*Max-Planck-Institut für Plasmaphysik, Garching, Germany,* [4]*MIT Plasma Science and Fusion Center, 77 Mass. Avenue, Cambridge, MA 02139, USA,* [5]*CEA, IRFM, F-13108 Saint-Paul-lez-Durance, France,* [6]*Department of Nuclear Engineering, Kyoto University, Kyoto, 606-8501, Japan,* [7]*CompX, Box 2672, Del Mar, CA 92014, USA,* [8]*XCEL Engineering Inc., 1066 Commerce Park Dr., Oak Ridge, TN 37830, USA,* [9]*LPP-ERM/KMS, Association Euratom-Belgian State, TEC Partner, Brussels, Belgium,* [10]*RRC Kurchatov Institute Tokamaks Physics Institute, Russia*

e-mail contact of main author: budny@princeton.edu

Abstract Benchmarking of full-wave solvers for ICRF simulations is performed using plasma profiles and equilibria obtained from integrated self-consistent modeling predictions of four ITER plasmas. One is for a high performance baseline (5.3 T, 15 MA) DT H-mode plasma. The others are for half-field, half-current plasmas of interest for the pre-activation phase with bulk plasma ion species being either hydrogen or He^4. The predicted profiles are used by seven groups to predict the ICRF electromagnetic fields and heating profiles. Approximate agreement is achieved for the predicted heating power partitions for the DT and He^4 cases. Profiles of the heating powers and electromagnetic fields are compared.

1. Introduction - Ion-cyclotron range of frequency (ICRF) power will be an important component of the ITER heating system. The planned heating power is 20 MW and the range of frequency is 40-55 MHz. Simulations of ICRF heating (and rotation and current drive) profiles are needed for estimating the effectiveness of the ICRF system in helping to create and sustain high fusion power. To get realistic plasmas for ICRF simulations and for performance predictions, integrated modeling is needed since the plasma profiles and applied heating are strongly coupled. Benchmarking of the codes used for simulating the heating is important for verifying and assessing confidence in the simulations and in the predictions.

Time-dependent integrated modeling needs to balance physics fidelity and numerical resolution with run speeds. Simulating some ICRF effects such as mode conversion, and some plasma regimes require much greater spatial resolution than others. Hence an important byproduct of benchmarking is an indication of the numerical resolution needed for accurate ICRF simulations, and also of the level of model sophistication needed to capture the important physics.

Several phases of plasma operation are planned for ITER. ICRF scenarios are discussed in Ref [1]. A pre-activation phase is scheduled for checking, testing, and calibrating the heating, diagnostics, stability control, fueling, exhaust, and safety systems. It will be especially helpful if the H-mode can be obtained in this phase for studying ELM effects and disruption control. There are indications that the H-mode might be achieved in hydrogen and He^4 - dominated plasmas with low field and density and with the planned heating power.

The auxiliary heating and current-drive systems being designed for the pre-activation and initial DT phases are negative-ion neutral beam injection (NNBI), ICRF, and electron-cyclotron range of frequency (ECRF). NNBI simulation codes have been extensively benchmarked for present experiments and for ITER [2, 3]. Likewise ECRF simulations have been benchmarked in present experiments and in ITER [4]. ICRF simulation codes have been benchmarked using profiles from existing experiments, but have not been thoroughly benchmarked for predicted ITER plasmas. The purpose of this paper is to benchmark the full-wave solvers used for ICRF simulations.

2. ITER plasmas for benchmarking - The benchmarking cases are listed in Table I. They include a high performance baseline (5.3 T, 15 MA) DT plasma (case 1), and plasmas for the pre-activation phase with half-field and half-current plasmas with either bulk H (cases 2 and 3) or He^4 (case 4). The PTRANSP code [5–7] is used to generate predictions for the plasma conditions. The PTRANSP

predictions are integrated and self-consistent in that the heating, beam current-drive, and beam torques are calculated using predicted plasma profiles. Several physics effects not yet included are the ICRF-induced current and rotation. These are included in the local flux-averaged energy, momentum, and magnetic field balance equations, and the time-evolution is predicted. The up/down asymmetric geometry of the flux surfaces are included. An example is shown in figure . The temperatures are calculated using GLF23 [8] and a pedestal model [9] incorporated into PTRANSP which predicts the pedestal pressure. The boundary values for GLF23 are the temperatures at the top of the pedestal. Temperature profiles are shown in figures 2. Case 2 is in L-mode and the others in H-mode. The PTRANSP runs typically use several hundreds of hours of CPU with about one-third of the CPU for TORIC (version 5) with a low number of poloidal modes (31). The runtime increases as the cube of the number of poloidal modes.

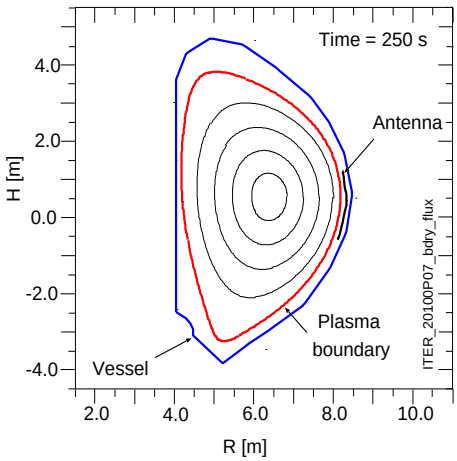

FIG. 1: Assumed boundary and computed flux surfaces for the DT case 1.

The ITER antenna design is composed of four columns of six short poloidal straps ($\simeq$ 0.27m).

case	case 1 (DT)	case 2 (H)	case 3 (H)	case 4 (He^4)
bulk ion species	DT	H	H	He^4
Impurity species	ash, Ar, Be	C	C	C
Fast ion species	D-beam, alphas	H-beam	H-beam	none
B_T [T]	5.314	2.678	2.665	2.665
I_p [MA]	15.0	7.5	7.5	7.5
$n_e(0)$ [$10^{20}m^{-3}$]	1.05	0.46	0.46	0.46
$T_i(0)$ [keV]	27.5	10	12	13.5
$T_e(0)$ [keV]	25	14	15	12.5
T_{ped} [keV]	5.3	1.5	2.5	1.8
β_n	2.0	1.5	1.8	1.2
P_{ICRF} [MW]	10.0	20.0	20.0	20.0
ICRF frequency [MHz]	52.5	52.5	52.5	42.0
minority species	He^3	He^3	He^3	H
n_{minor} / n_e	0.02	0.03	0.20	0.20
R_{res}-R_{axis} [m]	-1.488 (F1/2)	-1.368 (F1/1)	-1.590 (F1/1)	-0.305 (F1/1)
R_{res}-R_{axis} [m]	0.178 (S1/3)	0.364 (S2/3)	-0.096 (S2/3)	-0.305 (S1/2)
$E_{\|}$(minor) [MJ]	1.6	0.4	3.7	3.7
$E_{\perp}$(minor) [MJ]	3.4	1.5	10.0	9.5

TABLE I: *Summary of the benchmarking cases predicted by PTRANSP. Locations of two ion cyclotron resonances (relative to the magnetic axis) are listed along with ratios of Z / A of ion species with fundamental (F) or second harmonic (S) resonances within the separatrix.*

The top and bottom triplets of straps are driven in quadrature through an ELM-tolerant 3dB hybrid splitter. A simplified antenna is used for the PTRANSP predictions. It is assumed to extend poloidally 1.83 m, and is located 0.18 m outside the plasma boundary. The toroidal spectrum at the antenna is approximated by one node number $n_\phi = 27$, corresponding to k_ϕ is 4.229 m^{-1}. The equivalent parallel index is 3.843. The vacuum vessel is assumed to be perfectly conducting.

The auxiliary heating for the DT case 1 is assumed to start with 73 MW (the total planned for ITER), since the maximum may be needed to induce the transition to a high-performance H-mode. This power is composed of 33 MW of D-NNBI at 1 MeV, 20 MW ICRF, and 20 MW ECRF. The heating is stepped down as the alpha heating increases, thereby allowing the fusion gain Q_{DT} defined as the ratio of the fusion yield over the auxiliary and Ohmic powers to increase. The assumed thermal ion species

are D, T, He^4 ash, Be, and Ar impurities; the fast ion species are D-beams, and alphas. The electron density n_e is assumed to be flat, and the Be and Ar densities are assumed to be n_{Be} / n_e = 0.02 and n_{Ar} / n_e = 0.0012. The gas fueling, recycling, and ash transport is described in [7]. The plasma has $Q_{DT} \simeq 12$ at the benchmarking time (245s).

The predicted conditions for the pre-activation plasma assumes a shorter duration with the auxiliary heating of either 17 or 33 MW H-NNBI, 20 MW ICRF, and 20 MW ECRF starting at 50 s. The n_e profile is assumed to be flat and is ramped up to a peak of $4.6\times10^{19}m^{-3}$ by 80 s. The assumed ion species are H, C-impurity, and H-beams. The beam voltage is assumed to be 870 keV to avoid excessive power shine-through. Recent extrapolations of database values of the L→H power threshold scalings of the H-mode threshold in hydrogen (ex, [10]) indicate that the case with 17 MW will not achieve the H-mode. For this reason, case 3 is also considered with two beamlines delivering 33 MW of H-NNBI. This case appears to access the H-mode (barely) using [10].

Both the full field DT and half-field bulk H cases use the ICRF frequency of 52.5 MHz, and assume the minority ion species is He^3 at a density relative to the electron density of 2% for the DT and 3% for the pre-activation case. The He^3 absorption is at the fundamental frequency for the DT case and at the 2nd harmonic for the half-field case. He^3 heating is of interest for achieving a significant partition of the heating to thermal ion species, but it is considered optional for ITER. The ion partition increases with increasing He^3 density, but high He^3 density would dilute DT fuel. Also achieving large concentrations of He^3 in the resonance layer appears to be far too expensive for routine use. Another concern is that having a large partition of the heating to fast ion species may be undesirable due to causing excessive losses and TAE drive.

For the pre-activation bulk H cases the dominant absorption of ICRF power is via electron Landau damping (ELD), second harmonic heating of the He^3 minority with frequency twice the ion-cyclotron frequency ($\omega = 2\Omega_c$), and first harmonic heating of the majority H ($\omega = \Omega_c$). The second harmonic heating fraction is calculated to increase by increasing either the density or the energy of the He^3. Both are higher for the case 3 with 33 MW. Cases 2 and 3 (accelerating He3 at its second harmonic at reduced field) are numerical explorations of a heating scenario under assessment but currently not considered a main scenario for ITER. Experiments with this scheme using low concentrations of He^3 have been conducted in JET [12] and Tore Supra (Dumont, Private communication) The results have not been encouraging. In JET either low electron density (conducive to tail formation) or high He^3 concentrations ($\geq 15\%$) are needed in order to see increases in the ion temperature. Perhaps the heating power in these experiments was not sufficiently high to achieve high He^3 energies. PTRANSP predictions of stored energies of the minority ions for the cases are given in Table I.

Another pre-activation scenario is case 4 with H minority at half-field in a bulk He^4 plasma with fundamental absorption at 42 MHz. The rationale for this case is that it could be important for obtaining H-mode in the pre-activation phase. Scalings for the L→H power threshold in He4 plasmas are controversial, but some tokamaks report lower H-mode threshold in He4 than in H [11]. GLF23 predictions achieve moderately high central temperatures even with low pedestal temperatures, and achieve H-mode with the Martin scaling. Also, this case appears to be relatively easy case for benchmarking since indications are that this case will have strong single-pass absorption and will not have strong mode-conversion (which is not treated in some of the codes involved in the benchmarking).

3. Full-wave solvers - These PTRANSP predictions are used independently by seven groups to simulate the ICRF electromagnetic fields and plasma heating. The codes include TORIC (version 6) [13, 14], (version 5 is used for the PTRANSP-generated inputs for the simulations), AORSA [15, 16], CYRANO [17, 18], EVE [19], PSTELION [20], and TASK/WM [21]. Except for AORSA, all the codes are very similar. EVE has a different formulation of the wave equations. Some codes do not describe mode conversion. TORIC and PSTELION do. There are different choices of which distribution functions can be used to calculate the wave-equation coefficients: mono-Maxwellian, bi-Maxwellians, or a numerical distribution. A summary of approximations and numerical methods is given in Table II.

The predicted plasma profiles are provided for the full-wave codes as "plasma state" netcdf files. The equilibria inputs are provided as g-eqdisk files. An alternative set of ASCII input files are provided, with the equilibria in the form of Fourier poloidal moments specifying the (R,Z) values of constant

Code	FLR	Methods
AORSA	all orders	Fourier collocation in k_x, k_y, k_ϕ
EVE	2^{nd} order	Variation method; toroidal and poloidal modes; radial finite elements
CYRANO	2^{nd} order	Variation method; toroidal and poloidal modes; radial finite elements
PSTELION	2^{nd} order	Finite differences in radial coordinate
TORIC	2^{nd} order	Variation method; toroidal and poloidal modes; radial finite elements
TASK/WM	2^{nd} order	toroidal and poloidal modes; radial finite element

TABLE II: *Summary of full-wave solvers and their order of Finite Larmor Radii (FLR) approximations and numerical methods used.*

magnetic flux surfaces. Perpendicular and parallel energy densities of the minority, beam, and fast alpha ions are also specified in both forms. Their effective temperatures can be defined using either an isotropic profile:

$$T_{iso} = 2/3 \cdot (e_\perp + e_\parallel)/(n_{fast} \cdot Z_{fast} \cdot e), \tag{1}$$

or two anisotropic profiles:

$$T_\perp = e_\perp/(n_{fast} * Z_{fast} * e), \quad T_\parallel = 2 \cdot e_\parallel/(n_{fast} \cdot Z_{fast} \cdot e), \tag{2}$$

where n_{fast} is the fast ion density and $Z_{fast} * e$ is the fast ion charge. Profiles of $T_\perp$ and $T_\parallel$ for the minority ions are shown in figures 2.

Parameters needed for quantitative comparisons of the benchmarking results include the locations of resonance layers, zero-dimensional results such as the heating partitions, one-dimensional results such as heating profiles and electromagnetic fields along chords. Two-dimensional contours of heating and electromagnetic fields are very useful for giving insight about the solutions, and to check that the geometry and plasma profiles are being read in correctly by the full-wave solvers, but they do not lend themselves easily to quantitative comparisons. It is important to check the locations of resonance layers. Computing which locations are inside the plasma are complicated by the general shape of the boundary, and by the fact that in a time-evolving simulation the boundary can shift.

4. Fokker-Planck solvers - The minority heating and phase space distributions need to be predicted for accurate simulations. This is especially complicated in scenarios where the fast ions are resonant with the ICRF. In such cases, and also if finite orbit effects are important, Monte Carlo techniques may be needed for accurate coupling of the wave heating, but Monte Carlo techniques are very challenging in the presence of multiple fast-ion species. Various Fokker-Planck codes have been coupled to full-wave solvers. These can have drawbacks such as the necessity of averaging over banana orbits and loss of Finite Larmor Radius (FLR) effects. The Fokker-Planck module in PTRANSP (FPPRF) uses the up/down asymmetric equilibria, and the bi-Maxwellian assumption Eq. 2. Results for the predicted minority temperatures are shown in figures 2, and results for the heating are given in Table III. The CQL3D Fokker-Planck solver [22] computes the phase space distribution in energy and pitch angle, on an up/down symmetric equilibrium. Although benchmarking of the Fokker-Planck modules is not part of this paper, AORSA-CQL3S simulation results are included for comparisons with PTRANSP-FPPRF.

bulk ion species	DT case 1	H case 2	H case 3	He^4 case 4
P_{ICRF} [MW]	10.0	20.0	20.0	20.0
ICRF-electrons [MW]	3.7	11.1	3.9	4.0
ICRF-thermal ions [MW]	1.4	4.9	1.0	0.2
ICRF-minority [MW]	5.3	4.1	15.4	16.1
minority-electrons [MW]	1.2	1.8	10.5	10.2
minority-thermal ions [MW]	4.0	2.3	5.2	5.5

TABLE III: *PTRANSP-FPPRF results for heating powers of the ICRF, and for the minority species heating to the thermal plasma.*

Solver	T	thermal D	minority	He^4 ash	electrons	Ar	Be	D-beams	fast alphas
PTRANSP-bi	12.4	0.8	49.7	0.11	36.5 / 0.3	0.1	0.1	0.02	0.12
AORSA-iso	14.1	0.6	55.6	0.3	29.6	0.2	0.3	0.0	0.0
CYRANO	21.0	0.0	31.0	0.1	47.0	-	-	-	1.0
EVE-bi	12.5	0.4	48.8	0.1	36.8	1.1	0.2	0.0	0.1
EVE-iso	12.4	0.4	48.6	0.1	37.0	1.2	0.2	0.0	0.1
PSTELION	18.4	0.1	67.0	0.02	13.6 / 0.6	-	-	-	-
TASK/WM	15.2	1.1	48.4	0.03	25.7	-	-	-	-
TORIC-iso	16.0	0.5	51.2	0.03	31.7 / 0.7	-	-	-	-
AORSA-CQL3D	13.4	0.6	56.7	0.3	29.3	0.2	0.3	0.0	0.0

TABLE IV: *Comparisons of heating partitions (%) for the case 1 (DT) with n_{He^3}/n_e=0.02. CYRANO and PSTELION results are for a similar equilibrium. The PTRANSP results are from the runs generating the target profiles. The TASK/WM results are preliminary, for a similar equilibrium and profiles. The PTRANSP-bi, PSTELION, and TORIC-iso partitions to electrons are split to fast wave and Ion Bernstein Waves (IBW). The AORSA-CQL3D results are for comparison with PTRANSP-bi and the benchmarking results.*

Code	H	electrons	thermal He^4	carbon impurity
PTRANSP-bi	78.5	20.02 / 0.02	1.3	0.1
AORSA-iso	81.6	17.6	0.7	0.07
CYRANO-iso	75	25	2.0	<0.1
EVE-bi	73.7	25.2	1.0	0.1
EVE-iso	77.5	21.1	1.3	0.1
TORIC-iso	78.3	20.3 / 0.00	1.4	-
AORSA-CQL3D	74.3	24.0	1.5	0.2

TABLE V: *Comparisons of heating partitions (%) for pre-activation bulk He^4 case 4 with n_H/n_e=0.2. No beams are active in this case.*

5. Results for the fundamental harmonic cases 1 and 4 - The heating power partition among the plasma species depends sensitively on details such as the density and effective temperature of the He^3, which is sufficiently high in the DT case 1 for good ion heating. Results from the full-wave solvers, shown in Table IV, are in approximate agreement. Results for the heating partitions for the pre-activation case 4 in bulk He^4 plasma are also in approximate agreement, as shown in Table V.

The ICRF simulations indicate strong single-pass absorption for the first-harmonic cases 1 and 4. As indicated by the absence of rapid radial oscillations in plots from AORSA of the real and imaginary parts of $E_\alpha(R)$ (where the α unit vector is that part of the x unit vertor that is perpendicular to B) figure 3-a), mode conversion to propagating IBW is negligible for the DT case 1. This reduces the requirement of high numerical resolution. Simulations with the resolution increased beyond certain values produce nearly identical results, indicating the minimal resolution required for accuracy. The AORSA simulations are well-converged with a radial grid of 128×128. The TORIC simulations are well-converged with 255 poloidal modes and 803 radial zones. Comparisons of simulations of direct heating profiles for case 1 are shown in figure 4. The indirect plasma heating from the minority ions is not included. Examples of contours of $Re[E_-]$ from EVE are shown in figure 5-a).

6. Results for the second harmonic heating cases 2 and 3 - These cases are much more challenging since second harmonic heating is a FLR effect, and since single pass absorption is much weaker for these parameters. Plots from AORSA of the real and imaginary parts of $E_\alpha(R)$ for case 2 in figure 3-b) indicate that single pass absorption is weaker, and that mode conversion to propagating IBW's is negligible. Examples of contours of $Re[E_-]$ from EVE are shown in figure 5-b). Heating partitions for cases 2 and 3 are listed in Tables VI and VII. For case 2 a significant fraction of electron heating via damped IBW's is indicated. The differences found could be due to inadequacies in the treatment of the minority species, to lack of numerical convergence of the wave-solvers, or to the FLR approximation. The perpendicular and parallel energy densities of the minority ions specified for the wave-solvers are evolved in PTRANSP by FPPRF using effective tail temperatures. The AORSA-CQL3D result (using CQL3D

Code	He^3	electrons	thermal H	beam H	carbon impurity
PTRANSP-bi	29.1	42.1 / 7.0	21.4	0.4	0.0
AORSA-iso	23.0	69.4	7.5	N.A.	0.03
CYRANO-iso	31	64	5	N.A.	<0.1
EVE-bi	17.2	68.2	13.5	1.2	0.0
EVE-iso	15.6	68.9	14.5	1.0	0.0
TORIC-iso	9.7	66.3 / 11.3	12.1	1.0	0.0
AORSA-CQL3D	12.4	78.4	9.0	N.A.	0.03

TABLE VI: *Comparisons of heating partitions (%) for pre-activation bulk H case 2 with n_{He^3}/n_e=0.03. The PTRANSP-bi and TORIC-iso partitions to electrons are split to fast wave and IBW.*

Code	He^3	electrons	thermal H	beam H	carbon impurity
PTRANSP-bi	76.3	17.1 / 1.4	4.5	0.7	0.0
AORSA-iso	79.1	18.8	2.1	N.A.	0.1
CYRANO-iso	51	45	4	N.A.	<0.1
EVE-bi	45.2	37.7	9.2	7.9	0.0
EVE-iso	58.1	30.0	5.6	6.3	0.0
TORIC-iso	53.6	36.7 / 1.1	7.7	0.85	0.0
AORSA-CQL3D	64.0	30.0	5.9	N.A.	0.09

TABLE VII: *Comparisons of heating partitions (%) for pre-activation bulk H case 3 with n_{He^3}/n_e=0.2. The PTRANSP partition to electrons is further split to fast wave and IBW when available.*

for the minority distribution) is shown for comparison in the Tables. It is known that use of effective Maxwellian distributions are adequate for fundamental resonance heating [23, 24], but can over-estimate the tail for second harmonic absorption. This can get exaggerated as TORIC iterates with FPPRF. CQL3D can predict the He^3 phase-space distribution including the second harmonic He^3 cyclotron damping without assuming a form for the minority velocity distribution. The results in Table VI and VII show large differences between PTRANSP and AORSA-CQL3D, and even between AORSA-CQL3D and AORSA-iso. The source of these differences is under investigation and will be discussed in a future report.

On the other hand the TORIC-FPPRF and AORSA-CQL3D predictions for fundamental absorption in the cases 1 and 4 are much closer, suggesting the simpler treatment of fitting the energetic tail to mono or bi-Maxwellians may be a better approximation for the stronger single pass fundamental minority heating cases, or that the FLR approximation used in the full-wave solvers except for AORSA is less accurate in the 2nd harmonic scenario.

7. Discussion and conclusions - The benchmarking simulations find only small heating partitions to the impurity and fast ion species. Variations in the fraction of minority species are studied with some of the full-wave solvers. The results for the heating partitions for case 1 are in general agreement with the fraction of tritium heating increasing to $\simeq$40-50 % and the fraction to the minority decreasing to low values as the fraction of minority ion density decreases. Numerical convergence for case 1 is studied using AORSA, EVE, and TORIC. Results show that good convergence in the solutions is achieved with grids compatible with integrated, time-dependent prediction codes. Comparisons of the assumptions of mono-Maxwellian versus bi-Maxwellian minority temperatures are done using EVE for all four cases. The results show small (few%) effects in the heating fractions. The effects of including the up/down asymmetry for case are studied using PSTELION, which uses either a symmetric or an approximate up/down asymmetric geometry. Differences for the heating are small.

The benchmarking of full-wave solvers for the fundamental harmonic cases 1 and 4 give similar results, indicating that the solutions are reliable. Results for the pre-activation second harmonic cases 2 and 3 with bulk H have larger differences. The convergence of the full-wave solutions needs to be examined. Better solutions of the minority distributions are needed.

Acknowledgments - We wish to thank P. Lamalle, A. Polevoi, and J. Snipes for helpful suggestions

and comments. This work is supported in part by the US DoE Contract No. DE-ACO2-76-CHO3073.

[1] Gormezano, C., Sipps, A.C.C., Luce, T.C., Ide, S., *et al.*, Nucl. Fusion **47** (2007) S312.
[2] Houlberg, W.A., Gormezano, C., Artaud, J.F., Barbato, E., Basiuk, V., *et al.*, Nucl. Fusion **45** (2005) 1309.
[3] Oikawa, T., *et al.*, 22th IAEA Conference, Geneva **IT/P6-5** (2008).
[4] Prater, R., Farina, D., Gribov, Y., *et al.*, Nucl. Fusion **48** (2008) 035006.
[5] Budny, R.V., Andre, R., Bateman, G., Halpern, F., Kessel, C.E., *et al.*, Nucl. Fusion **48**, (2008) 075005.
[6] Halpern, F.D., Kritz, A.H., Bateman, . G., *et al.*, Phys. Plasmas **15** (2008) 062505.
[7] Budny, R.V., Nucl. Fusion **49**, (2009) 085008.
[8] Waltz, R.E., Staebler, G.M., Dorland, W., *et al.*, Phys. Plasmas **4** (1997) 2482.
[9] Onjun, T., Bateman, G., Kritz, A.H., and Hammett, G., Plasma Phys. Controlled Fusion **45** (2003) L55.
[10] Martin, Y.R., *et al.,* Journal of Physics: Conference Series **123** (2008) 012033.
[11] Ryter, F., Ptterich, T., Reich, M., Scarabosio, A., Wolfrum, E.,*et al.,* Nuclear Fusion **49** (2009) 062003.
[12] Lerche, E., *et al.*, 37th EPS Conf. Contr. Fusion and Plasma Physics, Dublin, June 2010, O4.121
[13] Brambilla M., Plasma Phys. Cont. Fusion **41**, (1999) 1.
[14] Wright, J.C., Bonoli, P.T., Brambilla, M., Meo, F., *et al.*, Phys. of Plasmas **11**, (2004) 2473.
[15] Jaeger, E.F., Berry, L.A., Harvey, R.H., Phys. Plasmas **15**, (2008) 072513.
[16] Jaeger, E.F., Berry, L.A., Lamalle, P.U., Loarte, A., Polevoi, A., *et al.*, APS DPP, Atlanta, (2009).
[17] Lamalle, P., PhD thesis - Université de Mons (1994) LPP-ERM/KMS Laboratory Report 101.
[18] Lerche, E., Van Eester, D., Krasilnikov, A., Ongena, J., *et al.* Plasma Phys. Control Fusion **51** (2009) 044006
[19] Dumont, R. J., Nucl. Fusion **49**, (2009) 075033.
[20] Vdovin, V.L., ICRF benchmarking modelling of ITER scenario No. 2, 7th Steady State Operation ITPA Topical Group meeting, Como, Italy, May 4-6, 2005.
[21] Batchelor, D.A., Beck, M., Becoulet, A., Budny, R.V., *et al.*, Plasma Sci. Technol. 9 (2007) 312.
[22] Harvey, R.W. and McCoy, M.G., IAEA Conf. Proc., Technical Committee Meeting on Advances in Simulation and Modeling of Thermonuclear Plasmas (Montreal, Canada, 15-18 June 1998) (Vienna, Austria: International Atomic Energy Agency) p 305.
[23] Stix, T., Nuclear Fusion **15** (1975) 737.
[24] Hosea, J., Bernabei, S., Colestock, P., Davis, S.L.,*et al.*, Physical Review Lett., **43** (1979) 1802.

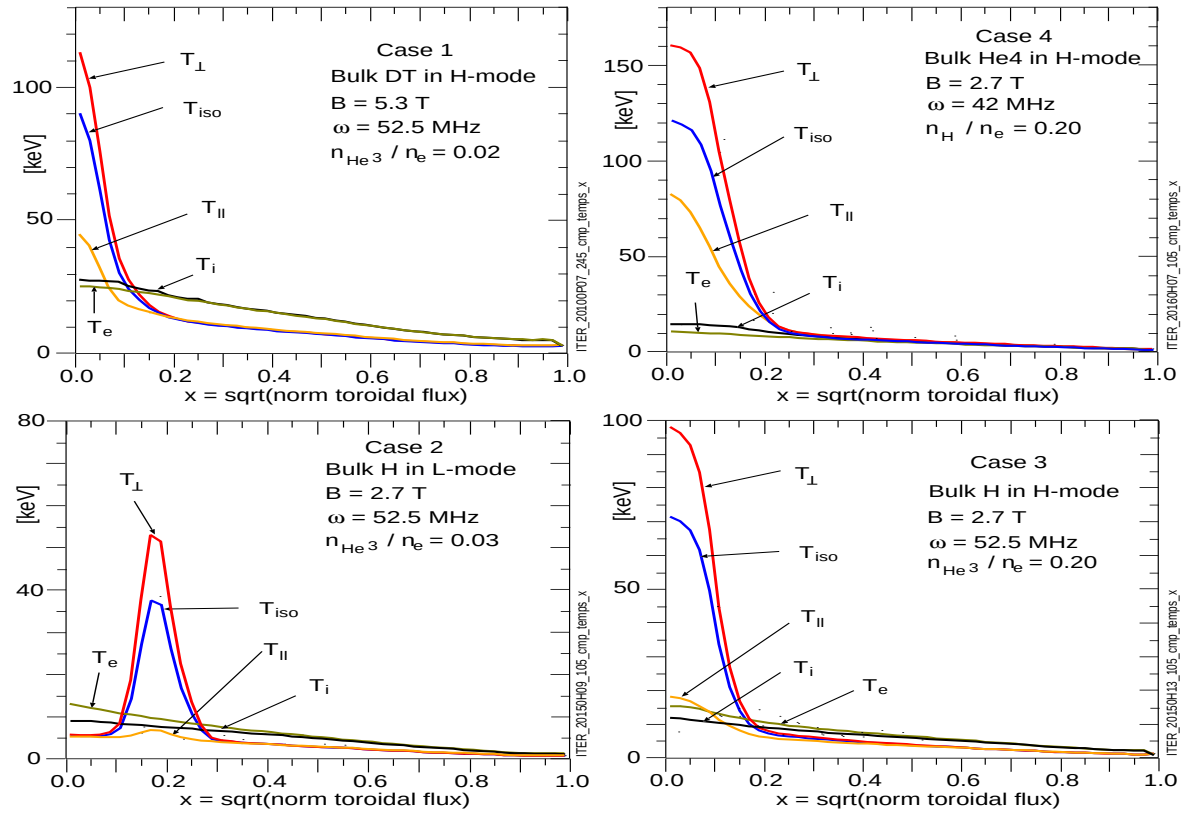

FIG. 2: Temperature profiles for the benchmark cases, computed from PTRANSP using GLF23 for the plasma and FFPRF for the minority ions using Eq. 2.

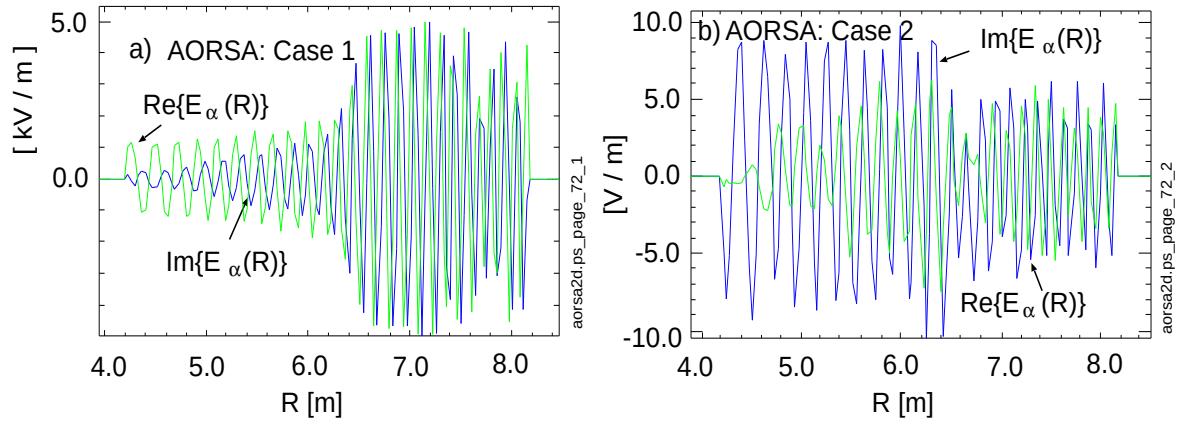

FIG. 3: AORSA-CQL3D simulations of E_α along the midplane for cases 1 (with fundamental resonance He^3) and 2 (with second harmonic He^3).

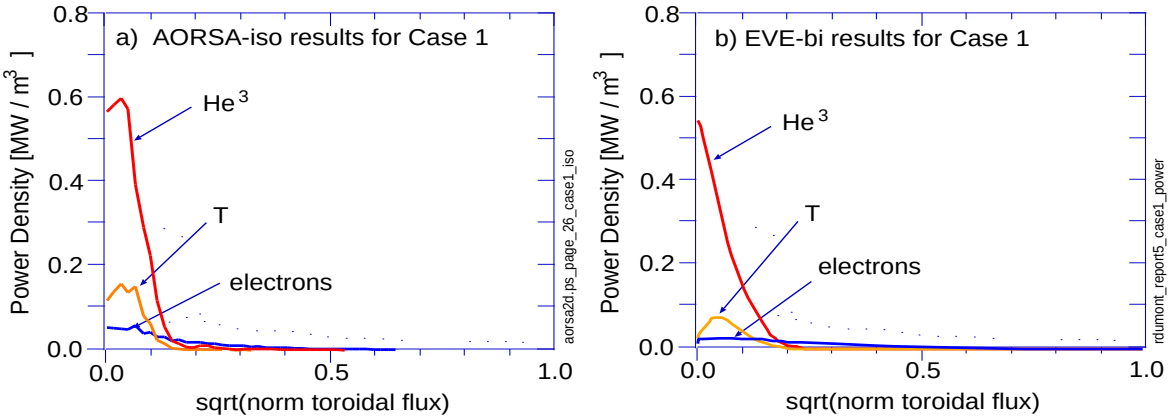

FIG. 4: Simulations of heating power profiles for the DT case 1 from AORSA and EVE.

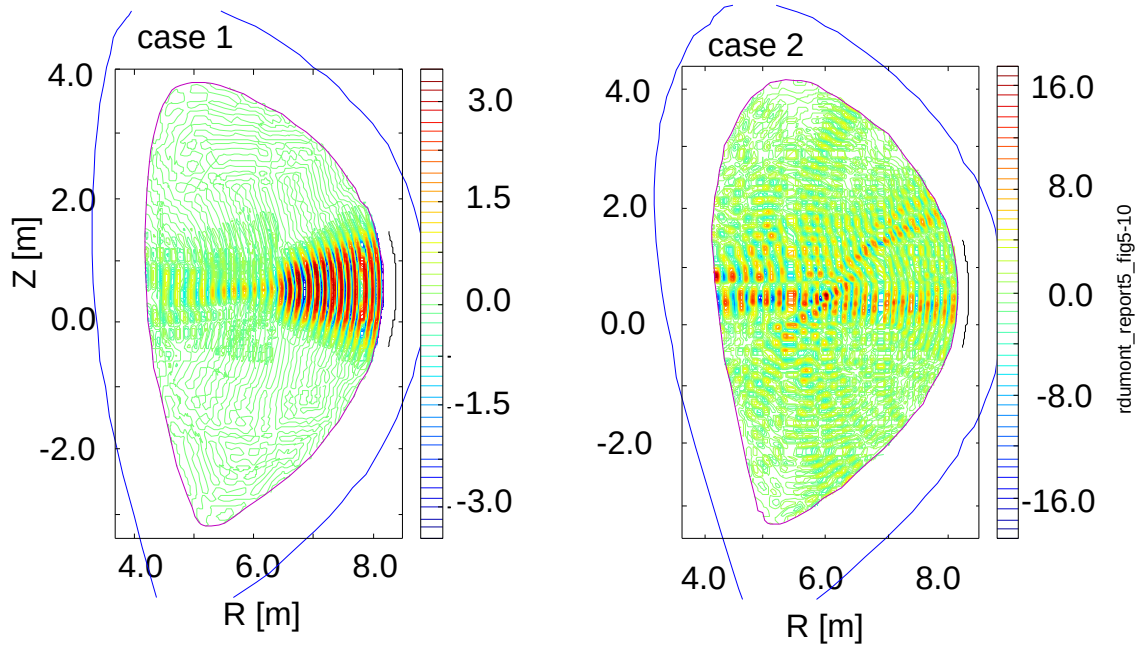

FIG. 5: EVE-iso simulations of contours of Re[E_-] for cases 1 and 2, in units of [kV/m] for the total coupled power. Single-pass absorption is stronger for case 1.